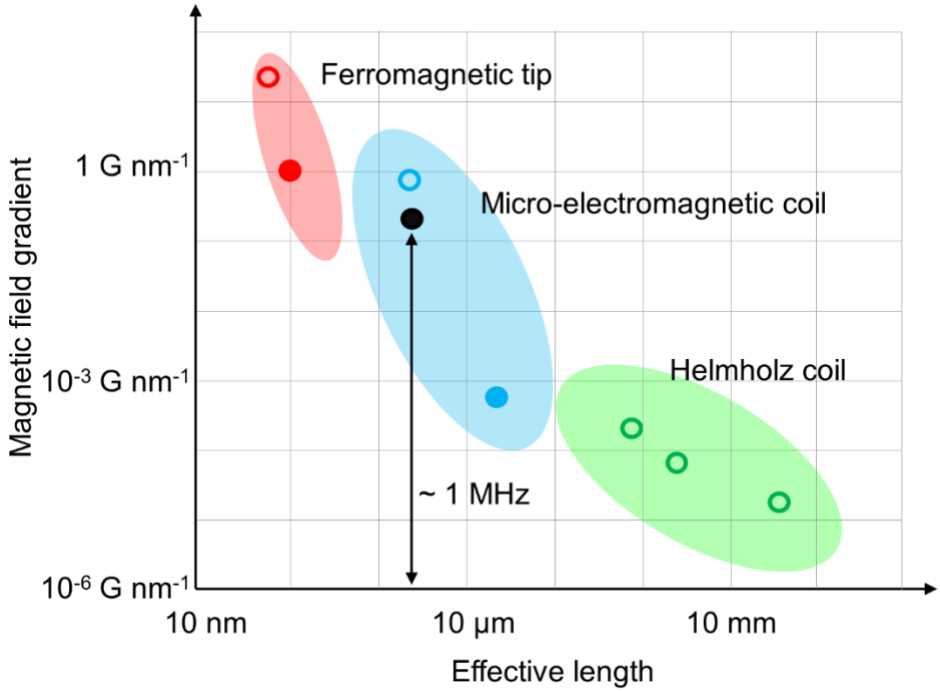
Supplementary information for "Selective addressing of solid-state spins at the nanoscale via magnetic resonance frequency encoding"

H. Zhang*, K. Arai*, C. Belthangady, J.-C. Jaskula and R. L. Walsworth

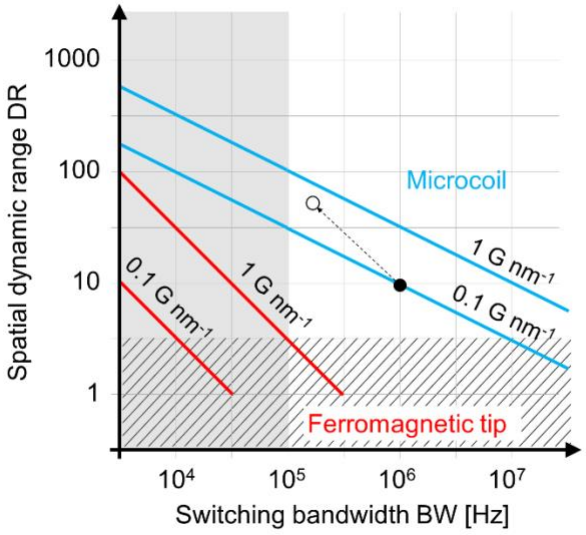
* These authors contributed equally to this work.

Supplementary Figures



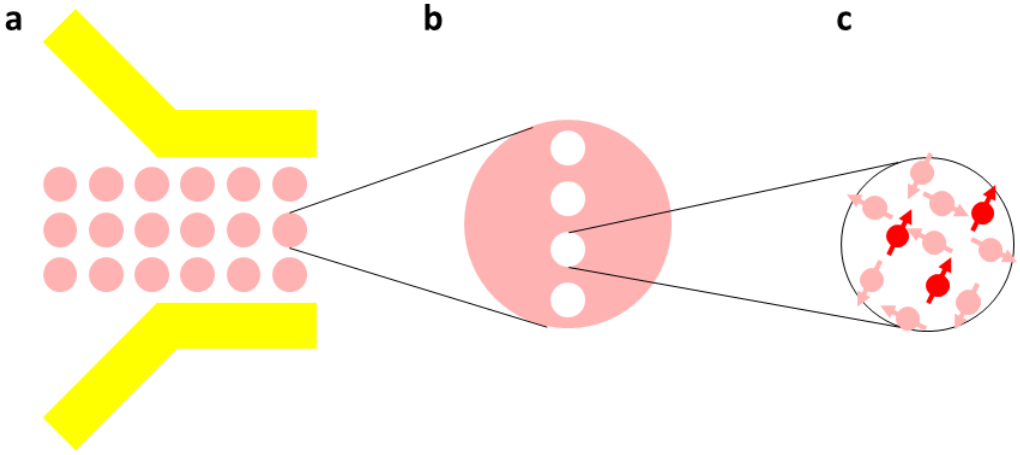
Supplementary Figure 1 | Comparison of selected magnetic field gradient techniques. Gradient strength as a function of effective length over which gradient magnitude applies. The open and filled circles indicate measurements at low temperature (< 77 K) and room-temperature, respectively. Ferromagnets (red) can produce the strongest gradients (>10 G nm^{-1}) at short length scales (<100 nm) [1-3]; however, switching the gradients requires slow mechanical motion of the magnet. Conventional Helmholtz and other 'volume' coils

(green), as used in MRI [4-6], can create gradients ~10^{-3} G nm^{-1} (= 100 T m^{-1}) over 100 mm. Micro-electromagnetic coils (blue) offer intermediate performance [7, 8]. Our device (back dot) provides gradients >0.1 G nm^{-1} that can be switched at ~1 MHz. The flexibility of microcoil design is useful for developing hybrid devices with microfluidic channels, Hall sensors, and microelectromechanical (MEMS) systems [9, 10]. These advantages make microcoils relevant for many applications, ranging from atomic manipulation [11, 12], to ferrofluid actuation [13], to manipulation of magnetotactic bacteria [14, 15] and DNA [16, 17].

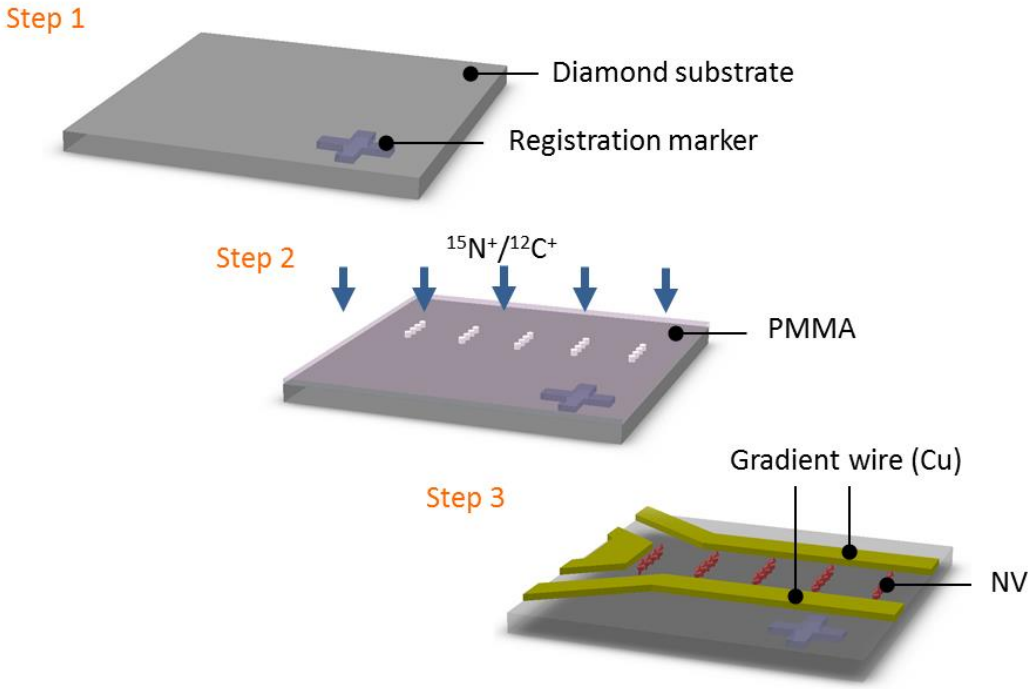


Supplementary Figure 2 | Spatial dynamic range and gradient switching bandwidth for site-selective NV control experiments. The spatial dynamic range is defined as DR = L/D, where L is the length scale across which the magnetic gradient is applied and hence NV sites can be selectively controlled, and D is the separation between individually addressable NV sites. DR < 2 (diagonal lines filled region) is not considered to be an array of distinct NV sites. The gradient switching bandwidth, BW, should be greater than the spin decoherence rate, which is ~100 kHz for typical dense NV samples (grey shaded region). The ferromagnetic tip and microcoil techniques are compared for two magnetic field gradient values, 0.1 G nm^{-1} and 1 G nm^{-1}, corresponding to D ≈ 100 nm and 10 nm, respectively, for selective addressing of neighbouring NV sites with high fidelity. For a microcoil, DR and BW are limited by the microcoil size and electric current and related through DR ~ $BW^{-1/2}$ (Supplementary Discussion 4). The values demonstrated in this work are DR = 10, BW = 1 MHz (black filled circle). By increasing the current to 1.4 A, DR = 24, BW = 160 kHz can be achieved (black open circle). A ferromagnetic tip can be mechanically moved at a typical speed of 100 μm/s to switch to another site or turn off the

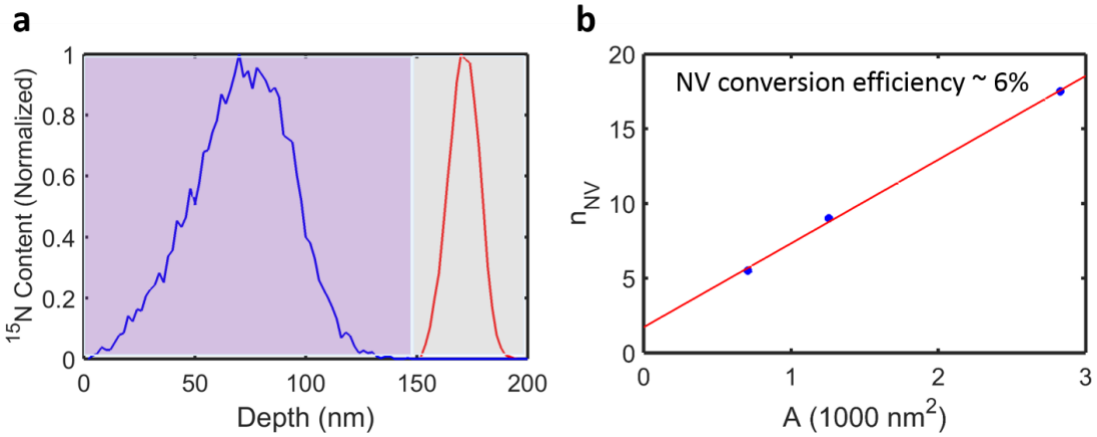
gradient. Thus, the switching rate is linearly proportional to the spatial dynamic-range (DR ~ BW^{-1}).



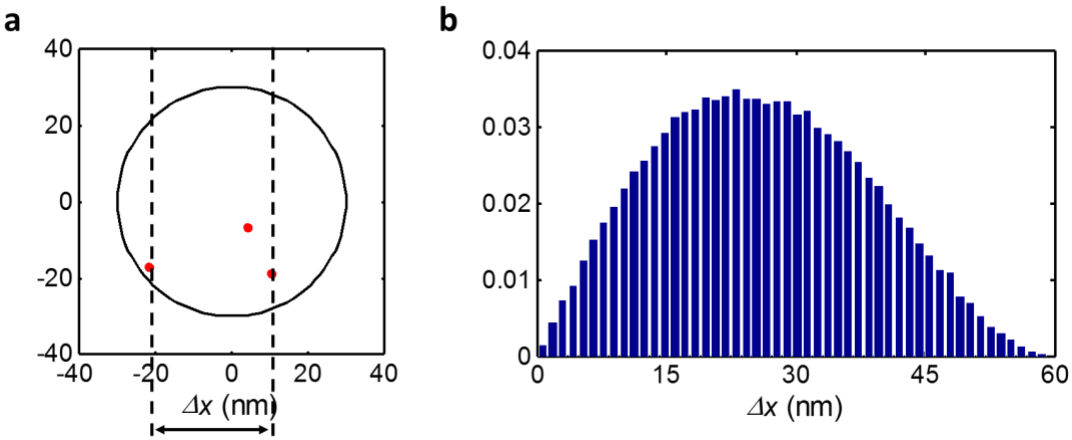
Supplementary Figure 3 | Three-level hierarchical structure of 2D NV arrays. The arrays of NV centres used in the present project can be described by a three-level hierarchical structure. **a**, The highest level is a 2D array of NV regions (~200 nm radius, 1 μm spacing), each of which can be individually optically addressed. **b**, The mid-scale level of a single NV region has four distinct NV sites (~30 nm radius, 100 nm spacing) aligned orthogonally to the microcoil wires, as shown in the zoomed-in view. Each NV site within a region can be selectively addressed via frequency encoding, as the NV ESR frequency becomes position dependent under the strong magnetic field gradient created by sending electric currents through the microcoil in an anti-Helmholtz configuration. **c**, At the smallest level, each site hosts multiple NV spins (typically 3±1 of a given orientation) with ~15 nm mean separation.



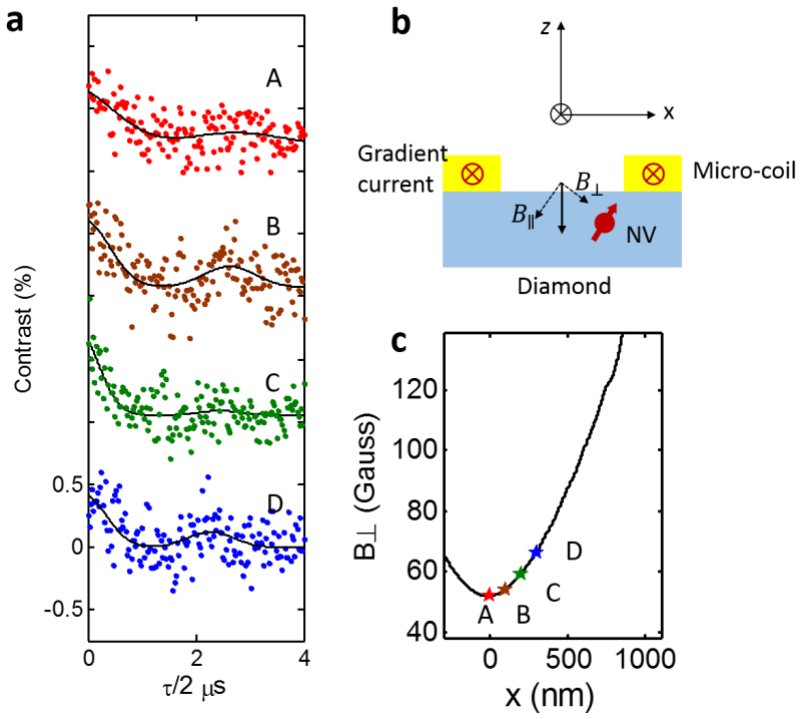
Supplementary Figure 4 | Three steps for fabrication of frequency encoding device. Step 1: Registration markers (cross mark) for alignment are fabricated on a diamond substrate with e-beam lithography and reactive ion etching. All subsequent fabrication uses the spatial coordinates defined by these markers. Step 2: A polymethyl methacrylate (PMMA) ion implantation mask is used to spatially control NV centre formation in a three-level hierarchical structure. In this work $^{15}N^{+}$ (10^{13} cm^{-2}, 14 keV) and $^{12}C^{+}$ (10^{12} cm^{-2}, 20 keV) co-implantation is implemented to enhance conversion efficiency from $^{15}N^{+}$ ions to NV centres. Step 3: After NV centres are created via high-temperature annealing (1200 ^{o}C, 4 hours), a Au microcoil is fabricated on the diamond and surrounding the 2D array of NV regions using e-beam lithography.



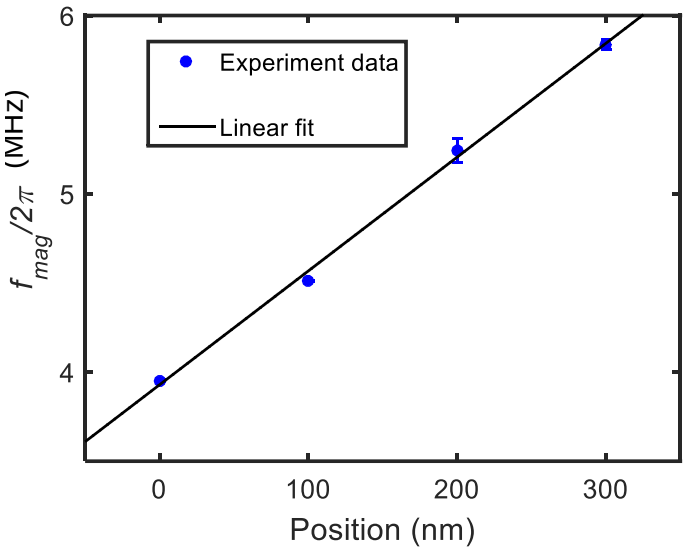
Supplementary Figure 5 | Characterization of ^{15}N implantation using PMMA mask. **a,** Simulated spatial distribution of implanted $^{15}N^+$ ions as a function of depth using the Stopping and Range of Ions in Matter (SRIM) program. The blue and red curves show the spatial profile of the resulting ^{15}N concentration formed by implanting $^{15}N^+$ ions through a PMMA mask (purple shaded area) and directly onto the diamond substrate (grey shaded area), respectively. When implanted through PMMA, more than 99.9% of $^{15}N^+$ ions are stopped within 150 nm from the PMMA surface and hence $^{15}N^+$ do not reach the diamond. The 150 nm thick PMMA (495 K C2) is formed with 3000 rpm spin coating. **b**, Number of NV centres (n_{NV}), determined from fluorescence count rate, is plotted as a function of the effective aperture area (A) with an ion implantation dosage of 10^{13} ions cm^{-2}. The estimated $^{15}N^+$ ion to NV centre conversion efficiency is 6%.



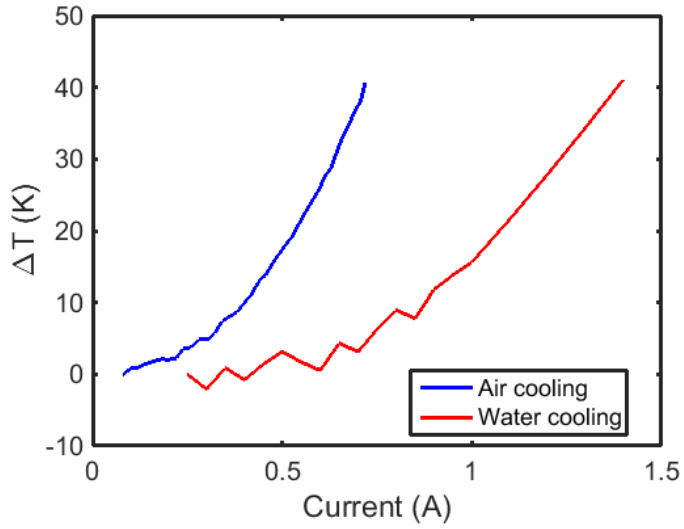
Supplementary Figure 6 | Randomly distributed NV centres inside 60 nm diameter aperture. a, Illustrative plot of three NV centres with random position distribution inside a 60 nm diameter aperture. Δx is the distance between the two NVs spaced the farthest apart. **b,** Representative histogram plot of distribution of Δx after 105 samplings of three NV centres randomly placed in the 60 nm aperture. This plot approximates the probability distribution function for Δx. The extracted standard deviation of 12 nm and mean value of 27 nm for Δx is qualitatively consistent with the observed NV ESR linewidth variation (as shown in main text Fig. 2b).



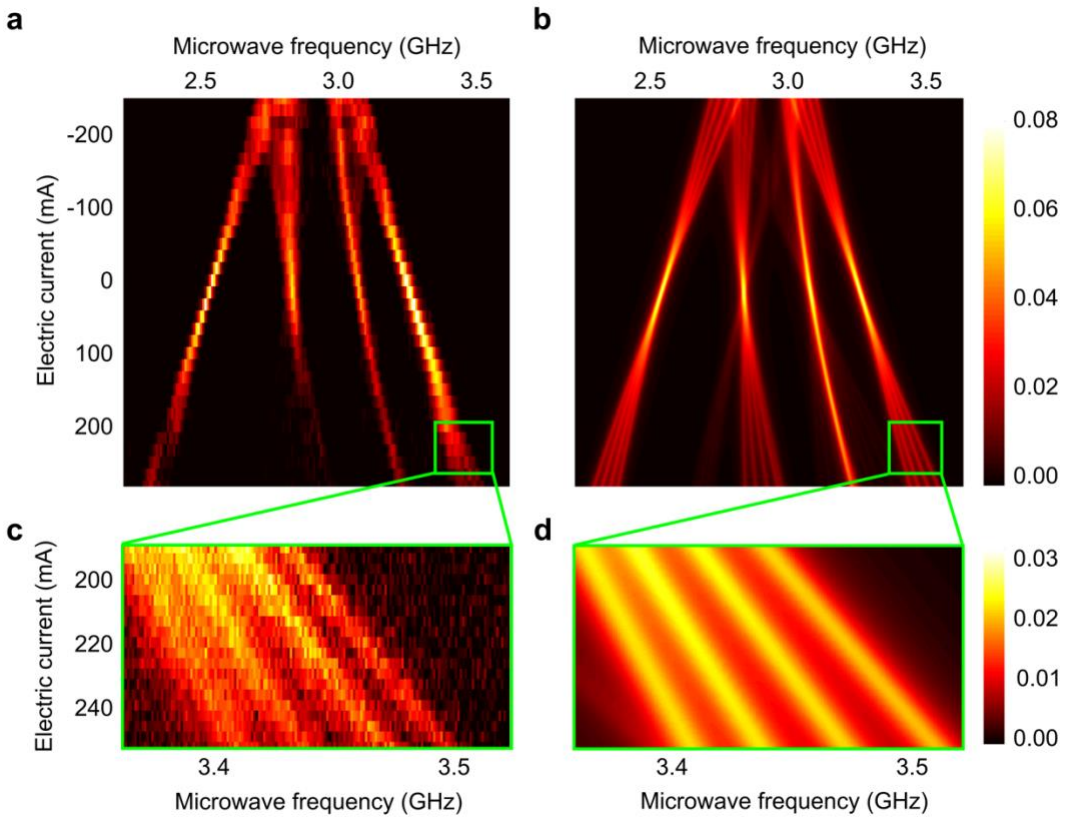
Supplementary Figure 7 | Site-selective NV spin Hahn echo measurements with applied magnetic field gradient. a, Measured NV Hahn echo signal as a function of half free precession time τ/2 with applied DC field gradient (red, brown, green, and blue traces correspond to NV sites A, B, C, and D). For each trace, the microwave frequency is tuned to address only one NV site, yielding NV T_2 = 3.8±1.7, 4.6±1.1, 1.8±0.6, and 3.8±1.0 μs for sites A, B, C, and D, respectively. Modulation due to the ^{15}N nuclear spin hyperfine interaction is observed, with different modulation frequencies across NV sites attributed to the varying transverse component of the applied DC field gradient ($B_\perp$). **b**, In the present experiment setup geometry, there is a finite angle between the NV crystallographic direction and the field gradient generated by the micro-coil, leading to $B_\perp$. **c**, COMSOL simulation of $B_\perp$ as a function of position (x). NV sites in site-selective Hahn echo measurements are labelled correspondingly.



Supplementary Figure 8 | Spatial frequency oscillations of site-selected 1D NV Fourier images. From the 1D NV k-space images in Fig. 3b of the main text, the coherent single-spatial-frequency for each NV site is extracted by fitting to a sinusoidal function. Error bars are estimated from the 95% confidence intervals of fitting. The spatial frequencies are linearly proportional to the NV position, which indicates the uniformity of the magnetic field gradient as expected.

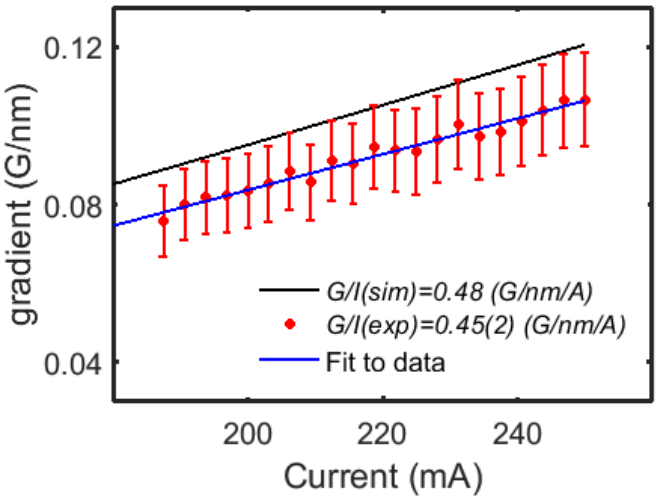


Supplementary Figure 9 | Microcoil heat test. To estimate the maximum current allowed in the field gradient device, the rise of microcoil temperature is measured as a function of electrical current by monitoring the change of resistance. When air cooling (shown as blue line) is used to dissipate heat from a heat sink attached to the NV diamond sample, the temperature increases by ~40 K with an electric current of 0.7 A, corresponding to a field gradient of ~0.3 G nm^{-1}. To further increase current, water is circulated on the heatsink. With the water cooling (red), the microcoil tolerates approximately twice the current (1.4 A), corresponding to a field gradient of ~0.6 G nm^{-1}.

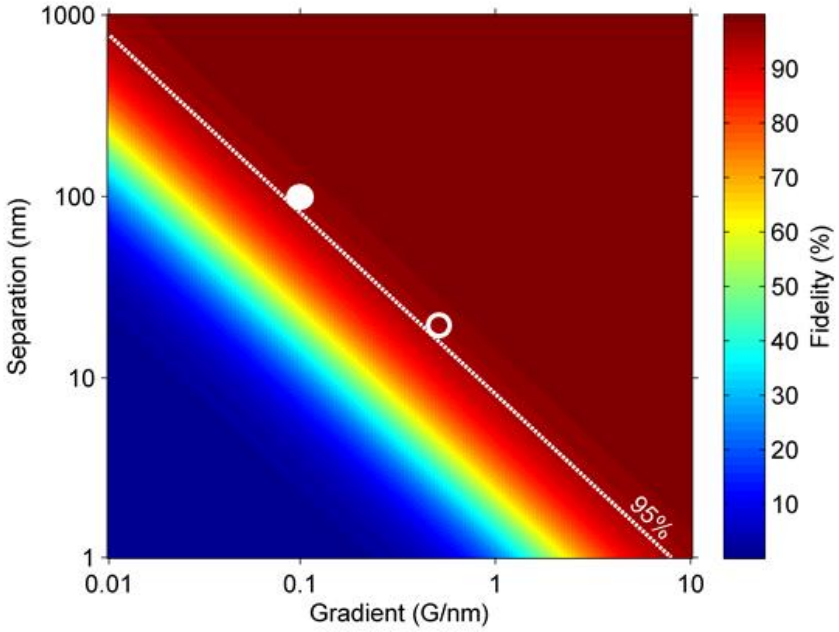


Supplementary Figure 10 | Effect of magnetic field gradient on NV ESR spectrum. **a**, Two-dimensional NV ESR spectrum measured by sweeping both the electric current through the microcoil (vertical axis) and the microwave driving frequency (horizontal axis). A permanent magnetic field of B_0 = 128 G along one class of NV orientations produces four bands of resonance peaks. The outermost and innermost two bands correspond to the transitions of the on-axis and three degenerate off-axis NV centres, respectively. As the electric current is increased, the resonance bands move with respect to each other. In particular, the inner two bands start to split into six. At larger current, only four bands out of eight have large contrast because the laser is linearly polarized and hence couples mostly to two NV axes. **b**, Simulated NV ESR spectrum. The magnetic field pattern is calculated at a fixed current of I = 250 mA using COMSOL. The field is assumed to be linearly proportional to the current. With the simulated field as an input, ESR resonance frequencies for all four NV orientations and four NV sites are determined by diagonalising

the NV Hamiltonian. **c**, Finer spectral resolution scan of the NV ESR spectrum with the sweep range indicated by the blue box in (**a**). The stronger the magnetic field gradient, the larger the splitting of ESR lines between adjacent NV sites (100 nm separation). **d**, Simulation corresponding to (**c**) and zoomed-in view of blue box in (**b**).



Supplementary Figure 11 | Magnetic field gradient as a function of microcoil current. NV ESR measurements are used to determine the magnetic field gradient as a function of electrical current (red dots), with a linear fit to the data (blue line) yielding the field gradient per unit current as $dB/dx/I$ = 0.45(2) G nm^{-1} A^{-1}. A numerical simulation of the field gradient produced by the microcoil (black line) gives $dB/dx/I$ = 0.48 G nm^{-1} A^{-1}. The disagreement between measurement and simulation could be attributed to the uncertainty of NV orientation with respect to the microcoil. Error bars on the data points are inferred from two factors: (i) 67% confidence interval of fitting each NV ESR spectrum to a sum of four Lorentzian lines; and (ii) uncertainty of NV centre position within each site in the array. In particular, the NV centres are assumed to be created randomly within the 60 nm diameter aperture of each array site, giving the standard deviation of NV location from the centre as σ = 15 nm.



Supplementary Figure 12 | Projected fidelity of site-selective NV Rabi driving. The fidelity of site-selective NV spin driving in the presence of a magnetic field gradient is calculated from $\Delta^2/(\Delta^2+\Omega^2)$, where $\Omega = 5$ MHz is the typical Rabi driving frequency, and $\Delta = \gamma D * dB/dx$ is the frequency detuning of the Rabi drive field between NV sites calculated from the gradient *dB/dx* and NV site separation D. The values used in this work are *dB/dx* = 0.1 G nm^{-1} and D = 100 nm (white filled circle), indicating a fidelity >95%. By water cooling, we expect to be able to drive NV sites separated by D = 20 nm using a stronger gradient of *dB/dx* = 0.6 G nm^{-1} (white open circle).

Supplementary Discussion

Supplementary Discussion 1: Microwave inhomogeneity

In Fig. 2d, a variation in Rabi frequency is observed across the four NV sites, which can be explained by the non-uniform microwave field distribution created by the antenna. The antenna + NV array system is in the microwave near-field; hence the spatial variation of the microwave field is determined by the dimensions of surrounding conductors rather than the wavelength of the radiation. Since the electric field is zero ($\mathbf{E} = 0$) in a conductor, no time-varying magnetic field exists in the microcoil according to the Maxwell-Faraday equation $\nabla \times \mathbf{E} = -\partial \mathbf{B}/\partial t$. Across the boundary between the microcoil and the surrounding medium, the normal component of the magnetic field B_y should be continuous. As a result, only a tangential component of the microwave field B_x exists near the microcoil boundary. This boundary effect alters the magnitude as well as the direction of the microwave field in the near field, which leads to a significant change in the NV Rabi frequency across the dimensions of the four-site array. Note that such microwave field gradients have also been used for selective addressing and motional-internal state coupling of atomic systems [19, 20].

Supplementary Discussion 2: Transverse magnetic field induced by gradient microcoil

The gradient field produced by the microcoil is nominally aligned with the uniform static field B_0 in order to perform NV frequency encoding and Fourier imaging. There is also a small transverse component to the gradient field $B_\perp(x)$, orthogonal to the direction of B_0, which is exploited for site-selective NMR spectroscopy of ^{15}N nuclear spins (Fig. 4 and

Supplementary Fig. 7). Thus, for the experimental protocol shown in Fig. 4a, the envelope of the NV Hahn echo signal in the presence of a DC magnetic field gradient is modulated as $S(\tau) \propto \sin^2(\omega_A t/2) \sin^2(\omega_B t/2)$, where $\omega_A \approx 2\pi \times 3$ MHz is the NV-^{15}N hyperfine coupling strength and $\omega_B \approx 14\gamma_n B_\perp$ is the ^{15}N nuclear spin Larmor frequency. Here $\gamma_n = 2\pi \times 0.43$ kHz G^{-1} is the gyromagnetic ratio of the bare ^{15}N nuclear spin, and the factor of 14 is an effective enhancement of this gyromagnetic ratio due to virtual transitions arising from higher order NV-^{15}N hyperfine interactions [18]. From the observed modulation frequency $\omega_B = 2\pi \times 0.36(2)$ MHz, the transverse field at NV site C is determined to be $B_\perp = 59(4)$ G, which agrees well with a COMSOL simulation of the gradient field produced by the microcoil (Supplementary Fig. 7c). Similar agreement between measurement and simulation is found for the other NV sites in the array.

Supplementary Discussion 3: Extension of selective addressing to multiple NV sites and spatial dimensions

In future work, straightforward methods can be used to extend selective control to two or more NV sites as well as a second spatial dimension. For example, multiple NV sites could be addressed simultaneously, in the presence of a frequency-encoding DC magnetic field gradient, by applying a microwave signal with spectral components at the NV ESR frequencies of all target sites. To selectively address a two-dimensional (2D) array of NV sites (e.g., a square lattice), one cannot simply employ simultaneous frequency-encoding gradients in both dimensions because a degeneracy of the resonance frequency occurs. Instead, one can maintain the spin polarization of a target row of NV sites, while dephasing the other rows; and then performing 1D frequency encoding along the target row to select the desired site. This procedure can be realized, for instance, by (i) putting all NV spins in

the 2D array onto the equator of the Bloch sphere with no DC gradient applied and a uniformly resonant microwave $\pi/2$ pulse; (ii) bringing only the target $x = x_0$ row back to the initial polarized state with a frequency-encoded $3\pi/2$ microwave pulse in the presence of a DC field gradient; (iii) waiting for T_2^* dephasing of the other (non-target) NV rows; and then (iv) performing 1D frequency encoding in the y direction to select the target NV site (x_0, y_0).

Supplementary Discussion 4: Microcoil performance

Maximum gradient strength and switching bandwidth

Though the frequency encoding demonstrations reported in the present work are performed with a maximum current of 250 mA, the gradient microcoil can be operated at a much higher current (and hence larger gradient strength) before it breaks down due to ohmic heating. The maximum current that the microcoil can support is determined by measuring the device temperature rise as a function of electric current (Supplementary Fig. 9). With water cooling, the temperature rises by nearly 40 K with I = 1.4 A, with a corresponding gradient of 0.6 G nm^{-1}. The switching bandwidth of the gradient pulse is determined by measuring the rising NV Rabi signal contrast as a function of delay between the initiation of the gradient pulse and $\pi/2$ pulse. Using impulse response function theory, the 3 dB switching bandwidth is $f_{3dB} = (\ln(0.9)-\ln(0.1))/(2\pi Tr) \sim 0.9$ MHz, where Tr = 400 ns is the measured 10%-90% rise time in the NV Rabi signal contrast.

Relation between spatial dynamic range and switching bandwidth

To characterize the maximum number of individually addressable NV sites, the spatial dynamic range of site-selective control, DR = L/D is introduced. Here L is the length scale across which the strong gradient is applied, and D is the separation between individually addressable NV sites. For a microcoil, L is determined by the separation between the two

wires and D is inversely proportional to the gradient strength. A magnetic field gradient of dB/dx = 0.1 G nm^{-1} and 1 G nm^{-1} corresponds to D ≈ 100 nm and 10 nm, respectively, assuming a Zeeman shift of about 30 MHz is needed for selective addressing of neighbouring NV sites with high fidelity. Since the gradient strength decreases quadratically as the coil separation increases ($dB/dx \sim I/L^2$) for a fixed value of gradient strength or D, the electric current I should be increased by $I \sim L^2 \sim DR^2$. However the maximum achievable current I is also limited by the switching bandwidth, i.e., $I \sim BW^{-1}$. BW can be affected by at least 3 factors: **a**, self-inductance of the micro-coil; **b**, peripheral circuits, such as in the printed circuit board (PCB) that interfaces the current source and micro-coil; and **c**, finite speed of the pulsed current source, which is a current amplifier in our case. COMSOL simulation indicates that the micro-coil has a very small self-inductance ~ 1 nH, and hence the corresponding bandwidth limit is on the order of GHz. Finite bandwith due to peripheral circuits can be, in principle, eliminated by integrating the current source close to the micro-coil. So the current amplifier is expected to be the primary switching bandwidth limitation. Furthermore, assuming that the output from the current amplifier is slew rate (SR) limited (which is usually the case when high current output or large voltage is needed), BW can be expressed as: $BW = SR/(2\pi V_p)$, where V_p stands for peak output voltage [21]. Since current is proportional to voltage, then BW and current are related as $I \sim BW^{-1}$. Thus we conclude that the spatial dynamic range and switching bandwidth are related via $DR \sim BW^{-1/2}$ (Supplementary Fig. 2).

Supplementary Discussion 5: Outlook for fabrication of high NV density arrays

High-precision nitrogen ion implantation is a key technical challenge for preparing either single NV centre arrays or strongly-coupled dense NV spin baths. Controlling the separation and number of NV centres with high precision remains an active area of research. It is thus of importance to evaluate the minimum limits of NV site area (A), NV-NV

separation within a single site (d), and spacing between sites (D), at the present state of technology. The NV site area is constrained by the mask diameter and lateral implantation straggle. Using a polymethyl methacrylate (PMMA) mask, apertures with diameter ≈ 30-60 nm can be created. Further reduction to 10 nm by reducing the mask thickness or even to ~1 nm by combining with atomic layer deposition of alumina may be possible; however, the lateral implantation straggle (7.0 nm at 14 keV implantation energy) will eventually limit the NV site area to $A_{min} \approx (10\ nm)^2$. Nevertheless, this is small enough for quantum information processing architectures based on spin chains with error correction methods [22 ,23]**.** The NV-NV separation within a single NV site is determined by the NV density. With an $^{15}N^+$ implantation dosage of 10^{13} cm^{-2} and N-to-NV conversion efficiency of 6 %, the diamond sample used in the present work has d = 15 nm. By increasing the implantation dosage and irradiating with neutrons or electrons, a minimum separation of $d_{min} \approx 4$ nm (corresponding to an NV-NV dipolar interaction strength ≈ 0.6 MHz) may be achievable, although the sample at this density might suffer from low fluorescence contrast due to NV^-/NV^0 charge state conversion and a shorter T_2^* due to remaining paramagnetic impurities. The spacing between NV sites, on the other hand, is limited by the NV site area, and thus cannot be smaller than $D_{min} \approx 10$ nm. If two NV centres are randomly picked from each of two NV sites with area A and spacing D, the mean and standard deviation of separation between them are given by ~D and $\sim A^{1/2}$, respectively.

Supplementary References

[1] Rugar, D., Budakian, R., Mamin, H. J. & Chui, B. W. Single spin detection by magnetic resonance force microscopy. *Nature* **430**, 329–332 (2004).

[2] Degen, C. L., Poggio, M., Mamin, H. J., Rettner, C. T. & Rugar, D. Nanoscale magnetic resonance imaging. *Proc. Natl. Acad. Sci. U.S.A.* **106**, 1313-1317 (2009).

[3] Mamin, H. J., Rettner, C. T., Sherwood, M. H., Gao, L. & Rugar, D. High field-gradient dysprosium tips for magnetic resonance force microscopy. *Applied Physics Letters* **100**, 013102 (2012).

[4] Glover P. & Mansfield P. Limits to magnetic resonance microscopy. *Rep. Prog. Phys.* **65**, 1489-1511 (2002).

[5] Lee, S. C., *et al.* One micrometer resolution NRM microscopy. *J. Magn. Reson.* **150**, 207-213 (2001).

[6] Seeber, D. A., Hoftiezer, J. H., Daniel, W. B., Rutgers, M. A. & Pennington, C. H. Triaxial magnetic field gradient system for microcoil magnetic resonance imaging. *Rev. Sci. Instrum*. **71**, 4263-4272 (2000).

[7] Drndic, M., Johnson, K. S., Thywissen, J. H., Prentiss, M. & Westervelt, R. M. Micro-electromagnets for atom manipulation. *Applied Physics Letters* **72,** 2906-2908 (1998).

[8] Lee, C. S., Lee, H. & Westervelt, R.M. Microelectromagnets for the control of magnetic nanoparticles. *Applied Physics Letters* **79,** 3308–3310 (2001).

[9] Lee, H., Liu, Y., Ham, D. & Westervelt, R. M. Integrated cell manipulation system—CMOS/microfluidic hybrid. *Lab Chip* **7**, 331–337 (2007).

[10] Florescu, O., Mattmann, M. & Boser, B. Fully integrated detection of single magnetic beads in complementary meta-oxide-semiconductor. *J. Appl. Phys.* **103**, 046101 (2008).

[11] Johnson, K. S., Drndic, M., Thywissen, J. H., Zabow, G., Westervelt, R. M. & Prentiss, M. Atomic deflection using an adaptive microelectromagnet mirror. *Phys Rev Lett* **81,** 1137–1141 (1998).

[12] Drndic, M., Lee, C.S. & Westervelt, R.M. Three-dimensional microelectromagnet traps for neutral and charged particles. *Phys. Rev. B* **63**, 085321 (2001).

[13] Beyzavi, A. & Nguyen, N.-T. Programmable two-dimensional actuation of ferrofluid droplet using planar microcoils. *J. Micromech. Microeng.* **20**, 0150118 (2010).

[14] Lee, H., Purdon, A. M., Chu, V. & Westervelt, R. M. Controlled assembly of magnetic nanoparticles from magnetotactic bacteria using microelectromagnets arrays. *Nano Letters* **4**, 995–998 (2004).

[15] Smith, M. J., Sheehan, P. E., Perry, L. L., O'Connor, K., Csonka, L. N., Applegate, B. M. & Whitman, L. J. Quantifying the magnetic advantage in magnetotaxis. *Biophysical Journal* **91,** 1098–1107 (2006).

[16] Chiou, C.-H. & Lee, G.-B. A micromachined DNA manipulation platform for the stretching and rotation of a single DNA molecule. *J. Micromech. Microeng.* **15**, 109–117 (2005).

[17] Chiou, C.-H., Huang, Y.-Y., Chiang, M.-H., Lee, H.-H. & Lee, G.-B. New magnetic tweezers for investigation of the mechanical properties of single DNA molecules. *Nanotechnology* **17**, 1217–1224 (2006).

[18] Maurer, P. C., *et al*. Far-field optical imaging and manipulation of individual spins with nanoscale resolution. *Nature Physics* **6**, 912-918 (2010).

[19] Ospelkaus, C., *et al*. Microwave quantum logic gates for trapped ions. *Nature* **476**, 181-184 (2011).

[20] Allcock, D.T.C, *et al*. A microfabricated ion trap with integrated microwave circuitry. *Appl. Phys. Lett.* **102**, 044103 (2013)

[21] P. Horowitz and H. Winfield, The Art of Electronics, 3rd ed. Cambridge University Press, 2015.

[22] R. Raussendorf and J. Harrington, "Fault-tolerant quantum computation with high threshold in two dimensions," Phys. Rev. Lett., vol. 98, no. 19, pp. 1–4, 2007

[23] D. S. Wang, A. G. Fowler, and L. C. L. Hollenberg, "Surface code quantum computing with error rates over 1%," Phys. Rev. A, vol. 83, no. 2, pp. 2–5, 2011.